Estimating the Effect of Stochastic Wind Stress Forcing on ENSO Irregularity

BRUNO BLANKE

Laboratoire d'Océanographie Dynamique et de Climatologie, Unité Mixte de Recherche, Centre National de la Recherche Scientifique, Paris, France

J. DAVID NEELIN

Department of Atmospheric Sciences and Institute of Geophysics and Planetary Physics, University of California, Los Angeles, Los Angeles, California

DAVID GUTZLER

Departments of Geography and Earth and Planetary Sciences, University of New Mexico, Albuquerque, New Mexico

(Manuscript received 20 February 1996, in final form 18 June 1996)

ABSTRACT

One open question in El Niño–Southern Oscillation (ENSO) simulation and predictability is the role of random forcing by atmospheric variability with short correlation times, on coupled variability with interannual timescales. The discussion of this question requires a quantitative assessment of the stochastic component of the wind stress forcing. Self-consistent estimates of this noise (the stochastic forcing) can be made quite naturally in an empirical atmospheric model that uses a statistical estimate of the relationship between sea surface temperature (SST) and wind stress anomaly patterns as the deterministic feedback between the ocean and the atmosphere. The authors use such an empirical model as the atmospheric component of a hybrid coupled model, coupled to the GFDL ocean general circulation model. The authors define as residual the fraction of the Florida State University wind stress not explained by the empirical atmosphere run from observed SST, and a noise product is constructed by random picks among monthly maps of this residual.

The impact of included or excluded noise is assessed with several ensembles of simulations. The model is run in coupled regimes where, in the absence of noise, it is perfectly periodic: in the presence of prescribed seasonal variability, the model is strongly frequency locked on a 2-yr period; in annual average conditions it has a somewhat longer inherent ENSO period (30 months). Addition of noise brings an irregular behavior that is considerably richer in spatial patterns as well as in temporal structures. The broadening of the model ENSO spectral peak is roughly comparable to observed. The tendency to frequency lock to subharmonic resonances of the seasonal cycle tends to increase the broadening and to emphasize lower frequencies. An inclination to phase lock to preferred seasons persists even in the presence of noise-induced irregularity. Natural uncoupled atmospheric variability is thus a strong candidate for explaining the observed aperiodicity in ENSO time series. Model–model hindcast experiments also suggest the importance of atmospheric noise in setting limits to ENSO predictability.

1. Introduction

The El Niño–Southern Oscillation (ENSO) phenomenon in the tropical Pacific is the most striking example of the natural climate variability on interannual timescales. Warm or cold sea surface temperature (SST) anomalies (e.g., Deser and Wallace 1990) and modification of the zonal slope of the thermocline for the ocean (e.g., Wyrtki 1985), modifications in the intensity and location of the main convection areas (e.g., Ropelewski and Halpert 1989), and large changes in the zonal wind intensity for the atmosphere (see Barnett 1985) are dominant features of ENSO.

Ocean–atmosphere coupled numerical simulations have been used thoroughly to investigate the physical mechanisms connected to its development. These include simple coupled models (e.g., Hirst 1986, 1988), intermediate coupled models (e.g., Zebiak and Cane 1987; Schopf and Suarez 1988; Battisti 1988), fully coupled general circulation models (e.g., Philander et al. 1992; Neelin et al. 1992; Latif et al. 1993), and hybrid coupled models (e.g., Neelin 1990; Barnett et al. 1993). These studies led to a better description of the phenomenon and an understanding of its underlying cyclic nature. The modeling view holds ENSO to be an oscillation with a period that depends on the dynamical adjustment of the subsurface ocean (Schopf and Suarez

Corresponding author address: Dr. J. David Neelin, Department of Atmospheric Sciences, UCLA, Los Angeles, CA 90095.
E-mail: neelin@atmos.ucla.edu

1990; Battisti and Hirst 1989). Recent analytical studies aimed at refining this and at understanding the relationship among various regimes (propagating modes or standing oscillations) found for simulated coupled variability (e.g., Wakata and Sarachik 1991a,b; Jin and Neelin 1993a,b; Neelin and Jin 1993). In most models, this oscillation grows as an unstable coupled mode (see Philander et al. 1984; Neelin 1991).

If ENSO is essentially cyclic, an obvious question is the source of its aperiodicity and, consequently, of barriers to its predictability. Though power spectra of ENSO time series have a broad spectral peak at 3–5 years consistent with oscillatory behavior (Rasmusson and Carpenter 1982; Rasmusson et al. 1991; Jiang et al. 1995), ENSO time series exhibit considerable irregularity. ENSO irregularity might arise from chaos within the slow components of the coupled system. Proposed routes to chaos have included period doubling (Münnich et al. 1991; Chang et al. 1994), interaction between modes (Mantua and Battisti 1995), and the interaction between ENSO inherent interannual variability and the earth's seasonal cycle (Jin et al. 1994; Tziperman et al. 1994; Chang et al. 1995; Tziperman et al. 1995; Jin et al. 1996).

Another plausible mechanism for aperiodicity includes forcing by uncoupled atmospheric variability. Zebiak (1989) suggested such effects were small. Penland and Sardeshmukh (1995) have recently argued from empirical models based solely on SST data that ENSO variability is due to several decaying modes maintained by atmospheric stochastic forcing. With an intermediate coupled ocean–atmosphere model, Kleeman and Power (1994) specifically addressed the issue of ENSO predictability limited by atmospheric noise, and suggested significant error growth in SST within only 4 months. This is comparable to the fastest timescale of error growth by deterministic coupled processes found by Goswami and Shukla (1991).

The role of uncoupled atmospheric variability on ENSO irregularity must be assessed quantitatively. The extent of the effect depends crucially on the magnitude and spatial properties of the noise estimate, as well as on the properties of the deterministic coupled model. Encouragingly, there is considerable agreement between the current study and simultaneous work by Eckert and Latif (1997) with an independent model. In this study, we emphasize that the atmospheric variability that exists independent of SST variations must be separated from the coupled component while preserving the spatial correlations of the noise, because the ocean is sensitive to the spatial structure of the forcing. We use in our study an empirical estimate of the noise that attempts to separate such coupled and uncoupled signals. The empirical atmosphere is derived from singular value decomposition (SVD) of the covariance matrix calculated from time series of pairs of interannual anomalies of observed monthly mean SST and Florida State University (FSU) pseudo–wind stress fields. The stochastic component of the wind stress forcing is based on the difference between observed wind stress and the part that may be attributed to SST through the SVD model. By construction, it maintains spatial correlations and has the same standard deviation as observations. The noise we define this way has little autocorrelation at lags longer than 1 month, and so the stochastic forcing for the coupled system is defined by random picks among monthly maps of this noise product. We evaluate the sensitivity of our ENSO model to this additional noise component in the wind stress forcing in cases with or without the inclusion of a prescribed mean seasonal variability.

Section 2 briefly describes the components of the coupled model. Section 3 describes the estimation of the stochastic forcing we use in this study. In section 4, the paper focuses on the effect of this additive atmospheric noise forcing on the simulation of a regular ENSO cycle. Section 5 addresses the possibility that such noise can sustain an otherwise decaying ENSO mode. Section 6 presents some results on predictability inferred from coupled noise experiments considered as forecasts of a model control run by other model runs. Section 7 describes a rough test of multiplicative noise. Conclusions are drawn in the last section.

2. Model

a. Hybrid modeling

The combination of a complex ocean model with a simpler atmospheric model for coupled interaction studies is now commonly referred to as a ''hybrid coupled model'' (Neelin 1990) or HCM. The fast adjustment of the atmosphere to changes (in SST) at the ocean surface motivates the use of a steady-state statistical or empirical model for the atmosphere. A more accurate representation of the oceanic dynamics is used since the ocean accounts for most of the memory of the coupled system. The main advantages of a hybrid coupled model lie in the subsequent easier understanding of the coupled mechanisms and in its low computing cost, with respect to a fully coupled general circulation model (coupled GCM), that allows the development of numerous sensitivity experiments.

Most HCMs make use of an ocean GCM (OGCM) coupled to a steady-state Gill (1980) type model as in Neelin (1990) or to a statistical model for the atmosphere built on empirical relations diagnosed between the SST and wind stress fields [with, e.g., point correlations as in Latif and Flügel (1991), or field to field relations using empirical orthogonal functions like in Barnett et al. (1993)]. A closely related version of the model used in the present study was introduced by Syu et al. (1995). Such HCMs aim at understanding ENSO variability by focusing on the physical coupled mechanisms and some are used as forecasting tools (Barnett et al. 1994).

b. The ocean model

As in Syu et al. (1995), the OGCM is basically version 1.0 of the GFDL modular ocean model. The domain is the tropical Pacific Ocean from 30°S to 50°N and from 130°E to 75°W, with the highest resolution used in the central Pacific (2° in longitude, 0.5° in latitude). The ocean floor is assumed flat, but realistic coastlines are included. There are 27 levels in the vertical, with most of them in the top 200 m (10-m resolution in the first 100 m).

The vertical turbulent mixing is diagnosed from Richardson-number-dependent vertical eddy diffusivity and viscosity coefficients, with analytical relations fitting the observations reported by Peters et al. (1988). The vertical penetration in the ocean of the solar radiation is taken into account, with a formulation including vertical extinction coefficients (Paulson and Simpson 1977).

c. The atmospheric model

Wind stress in the hybrid coupled model is produced by the ''SVDI'' methodology described in Syu et al. (1995). In this model a statistical estimate of the relationship between SST and stress anomaly patterns is derived from singular value decomposition (SVD) of the covariance matrix calculated from time series of pairs of observed monthly mean SST and pseudo-stress fields, with the observed climatological monthly means subtracted out from the data (for a review of the SVD algorithm, see Bretherton et al. 1992). The purpose of the SVDI model is to determine statistically optimized coupled modes of variability that can be used to define a field of wind stress anomalies using, as input, a field of SST anomalies. In this study we also consider the residual fields of stress (the portion of the observed stress not linearly coupled to SST anomalies). These fields are used as estimates of stochastic forcing for the coupled model, as described in section 3. As in Syu et al. (1995), observed monthly mean SST and surface pseudo-stress data (τ) for the period from January 1970 through December 1988 are used to derive the coupled modes. The SST data were analyzed at the U.S. National Meteorological Center using both in situ and satellite observations (Reynolds 1988). The τ vector fields were subjectively analyzed at the Florida State University (Legler and O'Brien 1984). Both SST and τ fields have been averaged onto a 187-point grid with 4° lat × 8° long resolution, covering the tropical Pacific basin between latitudes 20°N and 20°S. The two stress anomaly components u′ and v′ at each grid point are treated as independent scalar variables in the covariance matrix.

In the coupled model, and as in Syu et al. (1995), only the first seven modes that account for most of the observed covariability between SST and pseudo–wind stress are retained; they account for 68% and 34%, respectively, of the initial total variance of the SST and pseudo-stress time series. The covariance associated with subsequent modes drops off sharply. We use a drag coefficient $Cd = 1.2 \times 10^{-3}$ to convert pseudo stress into wind stress anomalies, with an additional multiplication by $\mu = 1.2$ (the coupling coefficient) before addition to the mean climatological wind stress (FSU analyses).

The atmospheric model provides the wind stress component of the atmospheric feedback. The surface heat fluxes are presented as a local linearization about the climatology (Oberhuber 1988), giving a restoring term to the observed climatological SST (Oberhuber 1988):

$$Q = Q_{\text{obs}} + (dQ/dT)_{\text{obs}} (\text{SST} - \text{SST}_{\text{obs}}), \quad (2.1)$$

where the value of $(dQ/dT)_{\text{obs}}$ is an estimate based on Seager et al. (1988).

Prescribed climatologies for the wind stress and the heat fluxes are either seasonal, or, in the case where the seasonal cycle is omitted, annual mean values. The SST used as the reference to diagnose SST anomalies in the coupled experiments is the mean seasonal or annual SST obtained when forcing the OGCM with the mean seasonal or annual value of the observed wind stress.

3. Estimate of the stochastic component

a. Space/time structure of observed stochastic forcing

The SVDI algorithm used to derive reconstructed stress fields for the hybrid coupled model is described in detail by Syu et al. (1995). As discussed in that paper, the zonal stress anomaly variance per grid point captured by SVDI from observed SST anomalies is 55 m^4 s^{-4}, while the total observed anomaly variance is 190 m^4 s^{-4}. Therefore, according to the SVDI model, the zonal stress anomaly accounted for by SST is 29% of the observed u′ variance. The 71% left as residual variance may be attributed largely to atmospheric internal variability and other mechanisms not explained by SST. The corresponding v′ variance captured by SVDI is 41%, leaving 59% as the residual. Locally, however, the fraction of total stress anomaly variance described by SVDI varies considerably.

Figure 1 compares the geographical distribution of u′ variability in the observed data with the variability associated with SST anomalies according to the SVDI model. The standard deviation of the data (Fig. 1a) exhibits a broad central Pacific maximum centered near the dateline and extending to the northeast and southeast from the equator, with minima near the equator in the far western and eastern parts of the basin. The standard deviation of u′ reconstructed from SVDI, shown in Fig. 1b, reproduces a more equatorially confined maximum in the vicinity of the date line with slightly less amplitude than in the data (as it must), with reconstructed zonal stress anomalies exhibiting only a small fraction of the observed variance poleward of 10° in either hemisphere. Thus, the map of the standard deviation of residual zonal stress anomalies (Fig. 1c) shows maxima

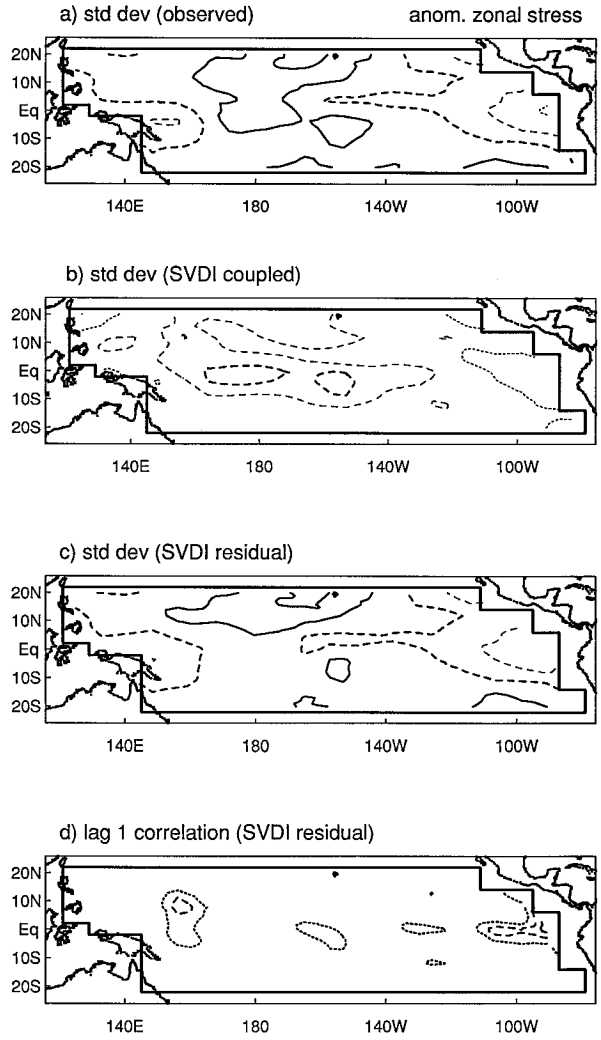

FIG. 1. Horizontal map of the standard deviation computed for the zonal wind stress anomaly over the period 1970–92. (a) Observations (pseudo-stress FSU analysis). (b) Atmospheric model forced by the observed SST. (c) Residuals: difference between observed stress and that attributed to SST forcing by the atmospheric model. Heavy solid and dashed contours are, respectively, 16 and 12 $m^2\ s^{-2}$; light solid and dashed contours are, respectively, 8 and 4 $m^2\ s^{-2}$. (d) Horizontal map of the 1-month lag correlation for the zonal residuals over the period 1970–92. Solid, dashed, and dotted contours are, respectively, 0.4, 0.3, and 0.2.

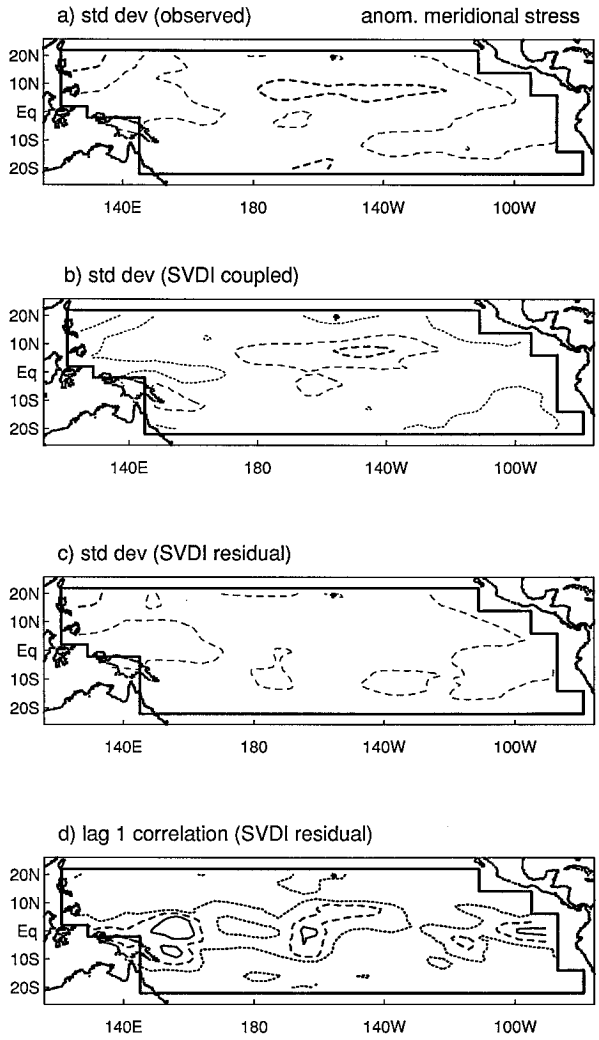

FIG. 2. As in Fig. 1 except for the meridional component of the wind stress.

in the subtropics of either hemisphere and an equatorial central Pacific minimum. A measure of the ''noisiness'' of the residuals is the one-month-lag autocorrelation of gridpoint residual values, shown in Fig. 1d. Off the equator the autocorrelation is less than 0.2 except along the eastern boundary of the domain and in a small patch near 10°N, 150°W. Several limited regions along the equator show autocorrelations between 0.2 and 0.3. These values are considerably less than the 0.4–0.5 autocorrelations typical of SVDI-reconstructed equatorial zonal stress anomalies (see Syu et al. 1995).

Figure 2 shows analogous statistics for meridional stress anomalies. Away from the basin boundaries the largest observed standard deviations occur along 10°N east of the date line. The variability produced by the SVDI reconstruction (Fig. 2b) has smaller amplitude in this region but reproduces the variance maximum in the right place. Large standard deviations are also observed along the southern edge and in the northwest corner of the domain, but most of this variability is neglected by SVDI and shows up in the residual fields. The map of v' residual variability in Fig. 2c suggests a band of maximum variability extending across the ocean just south of the equator. The one-month autocorrelation of v' residuals (Fig. 2d) shows much higher equatorial values than the analogous plot for u'. This could be due to the existence of atmospheric variability with longer correlation times in meridional stress than in zonal stresses. More likely, it may be that the meridional wind stress response to SST is more nonlinear than that of zonal stress and thus that the SVDI model misses part

TABLE 1. Correlations of the zonal (u′) and meridional (v′) pseudo–stress anomaly components with the Niño3 SST anomaly index (average over the eastern equatorial Pacific 6°S–6°N, 151°–87°W), for various locations. The correlations are given for the observed stress anomalies, the stress anomalies linearly related to SST according to the SVDI model, and the residual anomaly (observed minus SVDI).

u/v	lat/long	r (Niño3, obs)	r (Niño3, SVDI)	r (Niño3, resid)
u	Eq, 179°W	0.54	0.87	0.11
v	Eq, 179°W	−0.24	−0.63	−0.10
u	16N, 173°E	−0.16	−0.38	−0.02
v	16N, 173°E	−0.11	−0.32	−0.09
u	Eq, 149°E	0.08	0.41	0.19
v	Eq, 149°E	0.14	0.28	0.05
u	Eq, 99°W	−0.22	−0.13	0.19
v	Eq, 99°W	0.39	0.60	0.07

of this response to SST, which is then left in the residual. We thus have to accept the caveat that a portion of the residual meridional stress anomalies that we treat as noise may have either deterministic origins or longer decorrelation times.

Table 1 shows correlations of pseudo–stress anomalies at various locations with the Niño3 index, taken for the observed stress components and then for the components explained by SST and the residual, respectively. As expected, the component linearly associated with SST has much higher correlation with Niño3 than the observed stress in the regions where the ENSO signal is large, especially on the equator at the dateline. The residual correlations are low everywhere. This lends support to our contention that the residual can be used as an uncorrelated noise product.

Figure 3 shows the low-frequency portion of the power spectrum of u′ fluctuations at two grid points, one centered on the equator at 179°W (within the SVDI variance maximum shown in Fig. 1b), the other at 16°N, 173°E in the ''high noise'' region north of the equator in Fig. 1c. On the equator, the spectrum derived from observations contains a broad spectral peak at periods of 3 to 6 years. The spectrum of the SVDI model forced by SST reproduces this peak well, while it has less than the observed power at periods less than 36 months, as expected. The spectrum of residual zonal stress is reasonably white, with comparable power at all frequencies. For periods less than about 10 months essentially all the observed variance is contained in the residual (Syu et al. 1995), while at periods longer than 2 years the residual variance is considerably less than that attributed to SST. We remind the reader that a phenomenon with short decorrelation time has approximately a flat (white) spectrum at frequencies lower than the inverse of the decorrelation time. Thus, the presence of low-frequency signal in the residual is entirely expected and consistent with our later approximation of the stochastic forcing as white on timescales longer than a month. The partition of u′ variance between SVDI and its residual is much different at 16°N. The observed

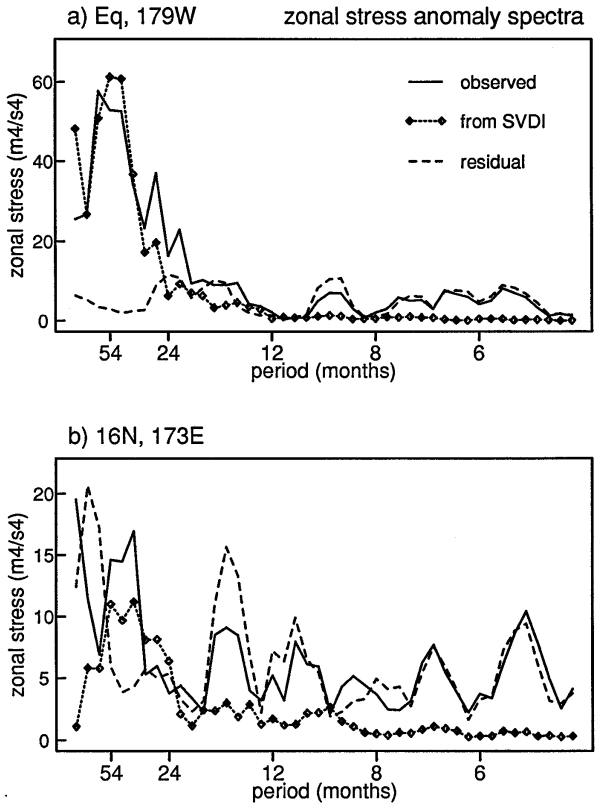

FIG. 3. Power spectrum of zonal wind stress anomaly fluctuations, for the observed pseudo stress (solid line), for the SVDI-reconstructed pseudo stress (dotted line and diamonds), and for the residual (dashed line): (a) on the equator, at 179°W; and (b) at 16°N, 173°E.

spectrum stills displays a modest 36–54-month spectral peak (note the expansion of the ordinate relative to panel a). Variability at the ENSO timescale is captured very efficiently by SVDI, and the 36–54-month spectral peak stands out much more clearly in the SVDI spectrum than in observations. The higher-frequency portion of the observed spectrum is not represented by the atmospheric model response to SST at all and shows up entirely in the residual spectrum. We note the caveat that there are apparent peaks in the residual spectrum; insofar as these are reliable, they are due to processes that we cannot account for. What we can capture is that there is power in the residual across all frequencies that is not attributable to tropical SST by our linear statistical model. This variance will be represented as a noise product that is white at periods in time longer than a month.

b. Implementation of stochastic forcing in the HCM

The datasets used to derive the SVDI model consist of 228-month time series of SST and pseudo–stress field anomalies. Using the singular vectors determined by SVDI, we generate monthly reconstructed zonal and meridional stress anomaly fields that retain only the portion of the stress linearly coupled to the underlying SST

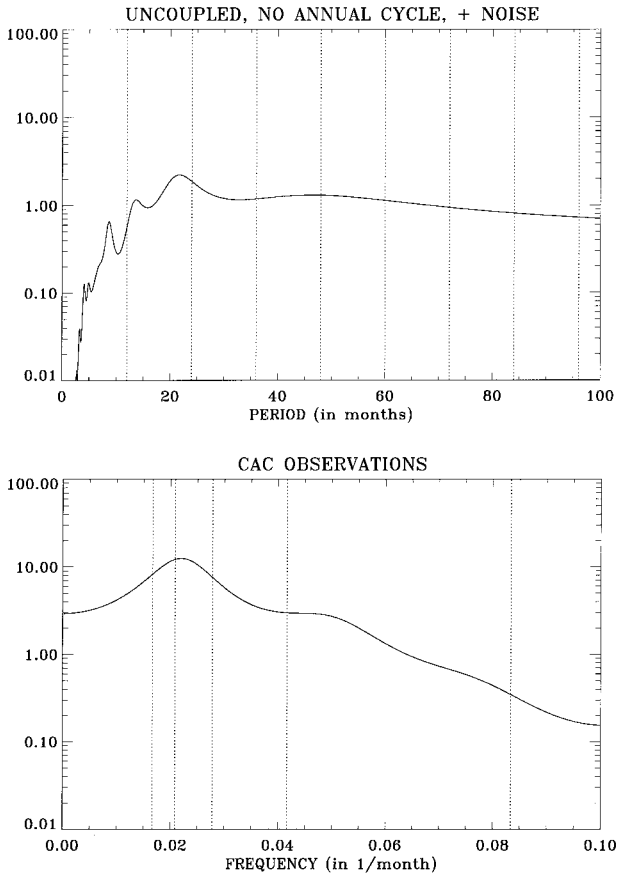

FIG. 4. Power spectrum of the Niño3 SST anomaly time series: (a) as a function of the period, for a 112-yr simulation with the OGCM only (uncoupled mode) forced by the empirically estimated stochastic wind stress product added to the mean annual observed stress; (b) as a function of the frequency, for the observations (period 1950–93). Spectra from the maximum entropy method (MEM) of order 30.

anomaly field. By subtraction from the original stress, we obtain the 228-month series of residual stress fields. To preserve the intrinsic spatial coherence of these residuals, we define our monthly stochastic forcing by entire residual fields chosen randomly among this 228-month sample.

For reference, we consider first the response of this noise product on the uncoupled ocean. A spectrum of the Niño3 SST anomaly (averaged over the box 150°–90°W, 5°S–5°N) obtained when forcing the ocean model with this noise added to the annual mean value of the observed stress is given in Fig. 4a. An approximately red spectrum for periods shorter than 12 months saturates to approximately white at longer periods. The maximum entropy method (MEM) has been used for all spectra shown hereafter. Spectra have also been computed by Fourier transform and multitaper methods for verification of essential features (not shown). MEM spectra have been computed for various orders of process to determine the order that gives reliable spectral peaks for the given length of series; order N = 30 is used in Fig. 4 et seq. For comparison, MEM spectra of monthly time series of the same length produced by a white noise process were examined for occurrence of spurious peaks (not shown). All spectra were computed using the toolkit of Dettinger et al. (1995). The peak at around 9 months in the ocean response appears reliable and is at the correct timescale for the lowest frequency ocean basin mode of the first baroclinic vertical mode (Neelin and Jin 1993). The power spectrum associated with the observed Niño3 SST anomalies over the period 1950–93 is given as a reference in Fig. 4b. For the order N = 30 MEM process used here, the ENSO peak at slightly less than four years may be seen, while the secondary ENSO peak sometimes noted at around two years (Rasmusson et al. 1990; Barnett 1991; Jiang et al. 1996) is less evident. The oscillatory nature of ENSO variability indicated by this peak is apparently not found in the uncoupled ocean spectrum of Fig. 4a.

4. Effects of added atmospheric noise on a regular ENSO cycle

We now examine the simulated ENSO in the coupled model with and without the addition of this estimate of atmospheric stochastic forcing. The modest computational cost of the HCM permits us to examine a number of multidecade runs (summarized in Table 2). We examine first cases in which the climatology is constructed using annual average climatological wind stress and heat

TABLE 2. Length (in years) and standard deviation for Niño3 SST time series from observations and HCM simulations (with or without prescription of the seasonal cycle, with or without added noise). The last row corresponds to an ocean-only experiment (coupling coefficient equal to 0).

	No seasonal cycle		With seasonal cycle	
	Length of the time series	Standard deviation	Length of the time series	Standard deviation
HCM without noise	48 years	1.12°C	56 years	0.68°C
HCM with noise				
$\mu = 1.2$	52 years	0.98°C	88 years	0.84°C
$\mu = 0.8$	41 years	0.80°C	/	/
Observations	/	/	44 years	0.82°C
OGCM with noise				
$\mu = 0.0$	112 years	0.53°C	/	/

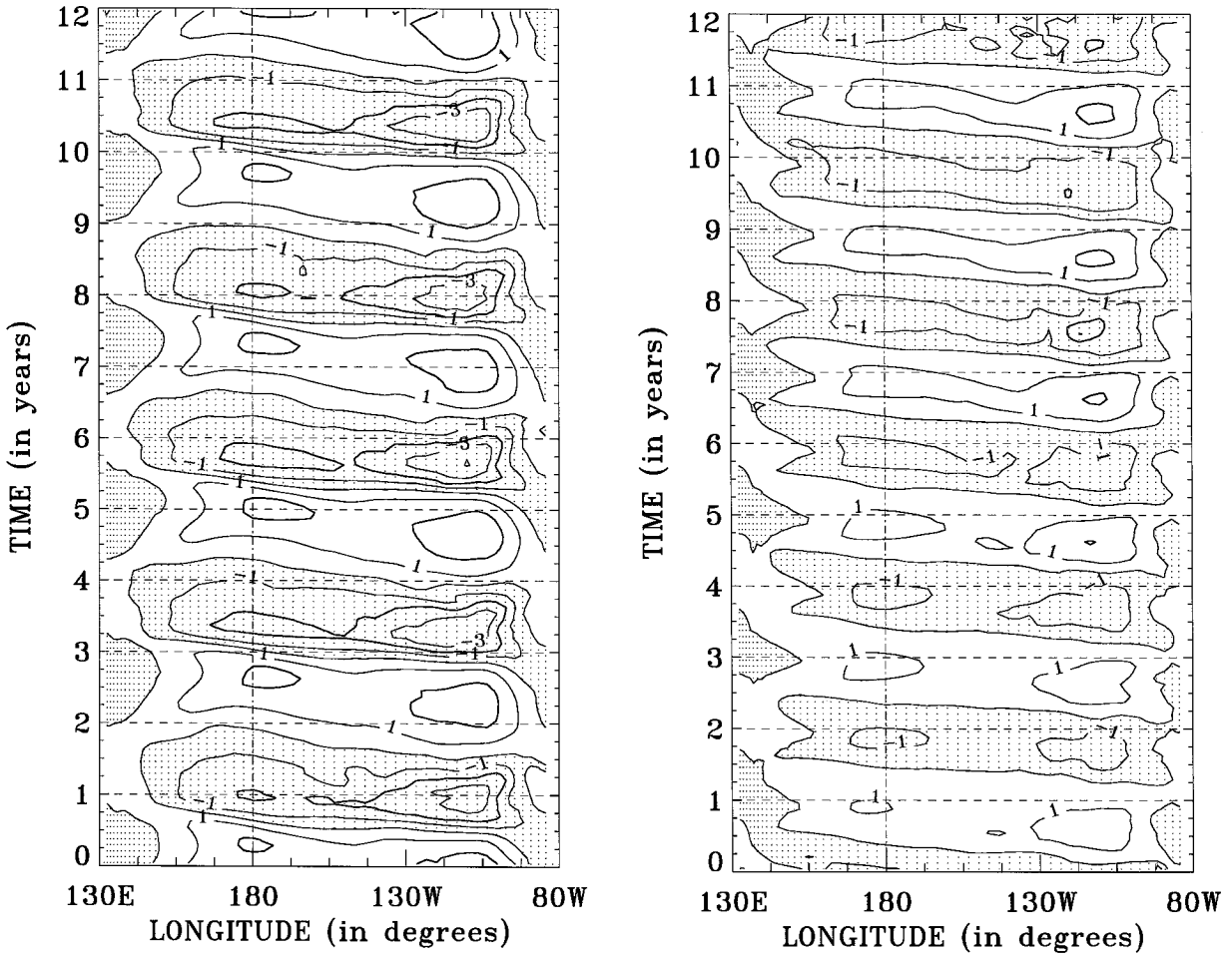

FIG. 5. Time–longitude diagram of equatorial SST interannual anomalies for the HCM. (a) Without seasonal cycle (pure interannual variability); and (b) with a prescribed mean seasonal cycle for the wind stress and the surface heat flux. Contours are 1°C, dotted regions indicate negative anomalies. Only a 12-yr subset out of the total experiment is shown.

fluxes, then cases in which the seasonal cycle is included in the climatology.

In these results, the spectral and other statistical characteristics of the variability are essentially independent of the initial conditions. For completeness, we note that coupled runs are started from multiyear ocean runs, either with or without annual cycle. The multiyear spinup helps avoid drift associated with adjustment of the deep ocean. Runs with the seasonal cycle begin in January. To quickly generate interannual variability of statistical equilibrium amplitude, the first month of each coupled simulation has an added westward wind stress anomaly in the western Pacific. This initial shock would correspond to about a 2.5°C anomaly for the Niño3 SST.

a. Pure interannual variability

We consider first the case with no seasonal cycle in the boundary conditions because the behavior is more complex when seasonal variability is included, and because the inherent period obtained for ENSO-like variability in the absence of seasonal cycle is an important indicator of a model's behavior. Figure 5a depicts the interannual variability for the equatorial SST over a 12-yr period selected out of the total integration. The spatial form is much as described in Syu et al. (1995), happening as a standing oscillation in SST with a period close to 30 months, with a hint of westward propagation. A hint of low-frequency variability is also visible, which is not well understood and is small enough to be ignored in this study. The overall temporal evolution is in reasonable agreement with known ENSO patterns, although the variability near the date line is slightly larger than canonical ENSO patterns from the 1970s and 1980s. Other results with the same hybrid coupled model have shown that the inclusion of a coupled feedback scheme for the shortwave radiation tended to reduce the variability in this region (Waliser et al. 1994). Other experiments (not shown), where the Oberhuber (1988) heat flux is replaced by a climatology chosen to give

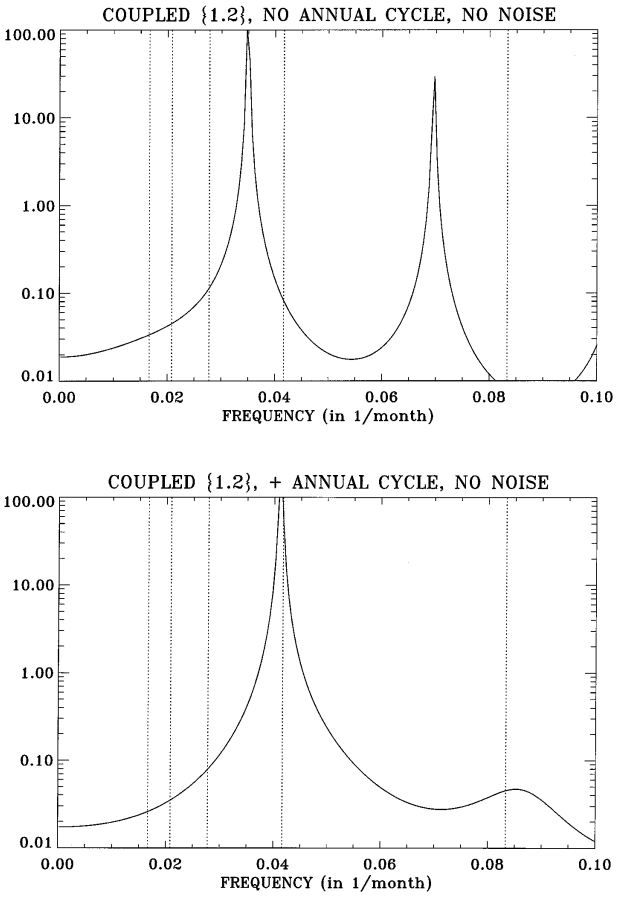

FIG. 6. Power spectrum of the Niño3 SST anomaly time series for the HCM: (a) for a simulation without seasonal cycle; (b) for a simulation with prescribed mean seasonal cycle for the wind stress and the surface heat flux. Time series length is 48 and 56 yr for (a) and (b), respectively, and MEM order N = 30 is used in both cases. Vertical dashed lines indicate periods of 5, 4, 3, 2, and 1 yr, respectively.

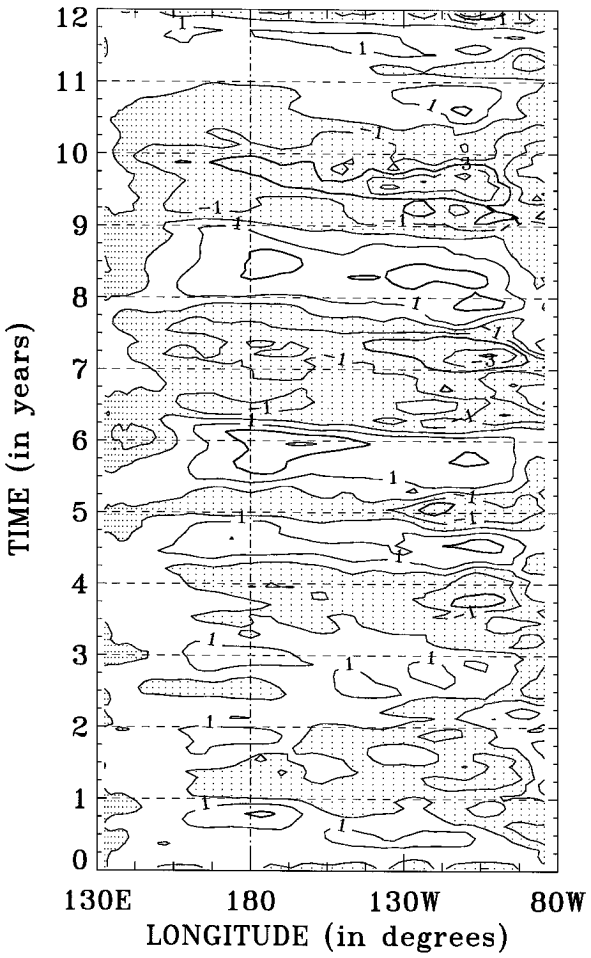

FIG. 7. As in Fig. 5b (case with seasonal cycle), except for a simulation with an added wind stress noise component.

closer agreement between simulated and observed climatological SST at the edge of the warm pool in the uncoupled model, show that this also reduces the variability near the dateline.

A spectral analysis of the Niño3 SST time series emphasizes the almost exact periodicity associated with the development of warm and cold events in the HCM. An MEM spectral analysis of monthly values of the Niño3 index leads to a single dominant spectral peak at 28.7-month period. The second harmonic of this peak may also be noted (Fig. 6a).

b. Inclusion of a prescribed seasonal cycle

The inclusion of a prescribed seasonal cycle for both the climatological wind stress and surface heat flux has no impact on the monotony of the simulated interannual variability but notably modifies the period of the oscillations: the development of cold and warm events looks very similar both in intensity and structure, but ENSO variability is now locked to a 2-yr period (Fig. 5b). Maximum and minimum anomalies of SST appear in early summer in the eastern Pacific while the variability peaks in late fall at the date line. Some longer timescale variability is also detectable in time series plots. However, spectra of the Niño3 anomaly time series (Fig. 6b) are dominated by a single spectral peak at the 2-yr period. This is simply a nonlinear shift of the inherent ENSO period seen in Fig. 6a to the nearest multiple of the annual cycle, namely 2 yr.

c. Coupled runs with stochastic wind stress forcing

To study the impact of added noise on the surface wind stress, multidecade coupled experiments are run for both cases, that is, without and with seasonal cycle included. The simulations are identical to the control runs described above except for the added noise component. The most obvious effect of the stochastic forcing is the much richer diversity obtained in the succession of cold and warm events. Figure 7 shows the time evolution along the equator for the case that includes the

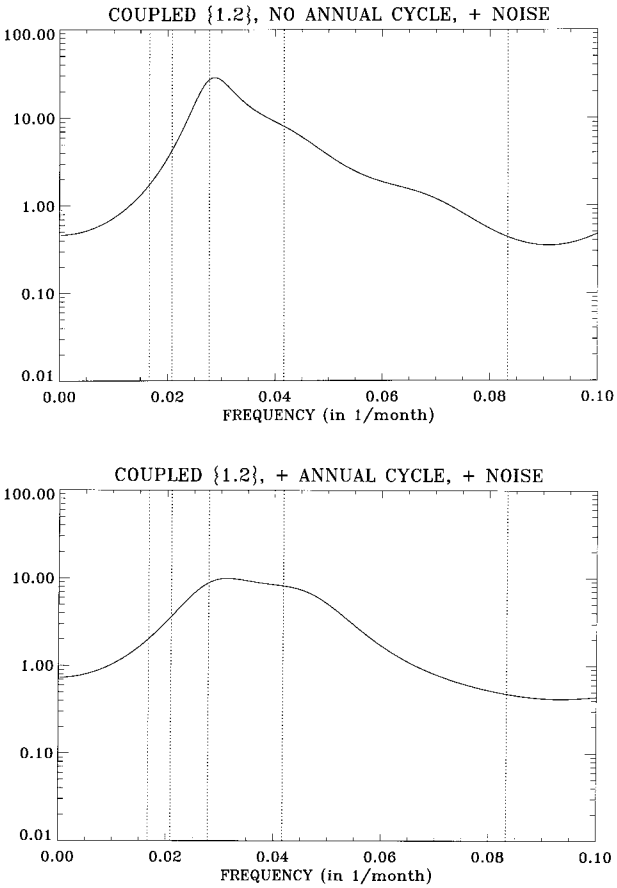

FIG. 8. As in Fig. 6 except for simulations with wind stress noise added: (a) spectrum for case without annual cycle; and (b) spectrum for case with annual cycle. Time series lengths are 52 and 88 yr, respectively.

seasonal cycle (the case without the seasonal cycle has similar features, so it is not shown). Some episodes are much larger than the amplitude of the periodic cycle in the control run, comparable to the largest observed ENSOs. Several episodes are weak, and sometimes warm (or cold) phases have much shorter duration, comparable to aborted ENSOs, and some have longer duration than in the control run. There is considerable variation also in the spatial patterns of the warm and cold episodes, with some episodes concentrated in the eastern basin and some with large westward extension. A more quantitative view of the irregularity in time of the interannual variability is given by the power spectrum of the Niño3 index (Fig. 8) for cases without and with seasonal cycle. The spectral peak associated with the model ENSO cycle is considerably broadened in both cases. In the case without annual cycle (Fig. 8a) the broadening is substantial. The half-width of the peak is more than 0.1 yr^{-1} (although this depends slightly on the MEM order). Furthermore, the peak has shifted to a somewhat lower frequency. Since this effect appears not to be simply due to the addition of a red background, we presume that nonlinear effects of the noise upon the cycle must be responsible. In the case with annual cycle, the broadening is even more dramatic, and there is a clear shift toward longer periods. Whereas the control run with annual cycle had its period shifted to lock to exactly 2 yr, the peak in the noise-forced case spans the whole 2–3-yr range. In general, for periodically forced systems (Iooss and Joseph 1990), and in particular for ENSO (Jin et al. 1996), frequency locking to nonlinear subharmonic resonances at integer multiples of the external frequency can occur over substantial regions of parameter space. The peak broadening seen in Fig. 8b is consistent with a tendency for the stochastically forced system to visit subharmonic resonances at both 2 and 3 yr, to either side of the model inherent ENSO period at 2.4 yr.

d. Preferential seasonal phase for simulated ENSOs

We now diagnose whether the newly generated ENSO events are randomly spread along the calendar year or still locked on a preferential seasonal phase, as documented by observations (Rasmusson and Carpenter 1982). We compare observations of the Niño3 SST anomaly index with the one obtained from the model. All time series are normalized by their respective standard deviation, and we define warm or cold periods by normalized SST anomalies greater or lesser than 0.5. We then sum for each month of the calendar year the occurrences of warm or cold events. This makes sense because the timescale of a given warm or cold phase is likely to last less than one year, except in very unusual episodes like the 1982–83 El Niño. The histogram for each month (Fig. 9) is finally normalized so the average over all calendar months is unity. Thus, a value larger than one indicates a preferential period for the development of anomalous episodes. The observations for the period 1950–93 are used.

Results for the HCM run with stochastic forcing show there is still a seasonal dependence for the development of warm and cold phases. The added noise disrupts the period locking but a specific phase of the annual cycle is still preferred. The model is characterized by a minimal number of warm or cold occurrences in late winter and early spring, just like the observations. The increased likelihood of warm occurrences (Fig. 9b) in the Niño3 region by this criterion is found in May through October in observations and the model conforms to this reasonably well, though with peak probability slightly earlier in the season. Cold occurrences (Fig. 9a) in observations are preferred during May–January, and again the model tracks this general behavior, though it misses the details of the two independent peaks (late spring and fall) found in the observations.

The same analysis applied to the HCM without stochastic forcing roughly provides a similar likelihood, though of course more accentuated because of the exact period locking. Thus, the preferred phase of ENSO in

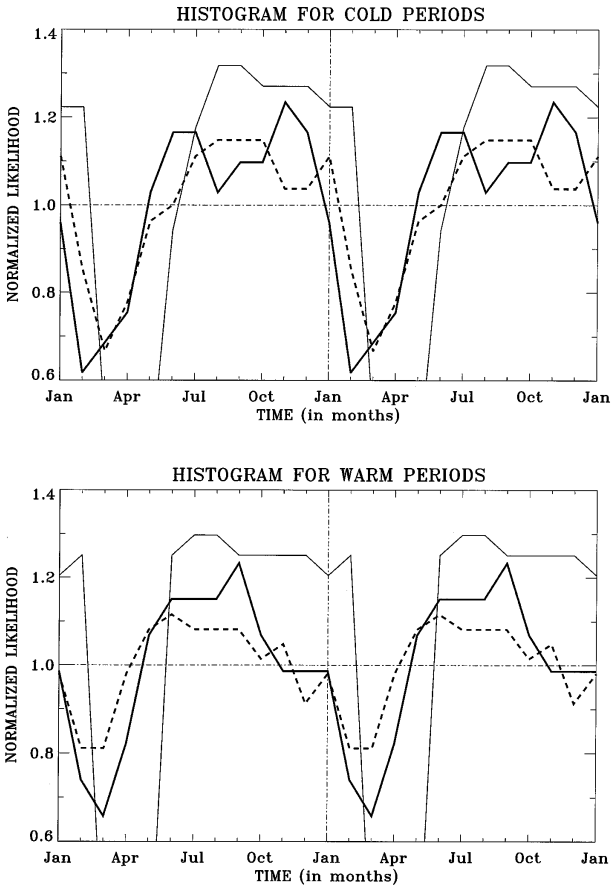

FIG. 9. Histogram of occurrences of an anomalous event as a function of the calendar month for observations during 1950–93 (heavy solid line), for the HCM with an added wind stress noise component (heavy dotted line), and for the HCM without noise (light solid line): (a) for cold events; (b) for warm events. Values larger than one indicate enhanced probability Niño3 SST anomaly exceeding 0.5 standard deviations. The data is repeated through a second calendar year for ease of viewing.

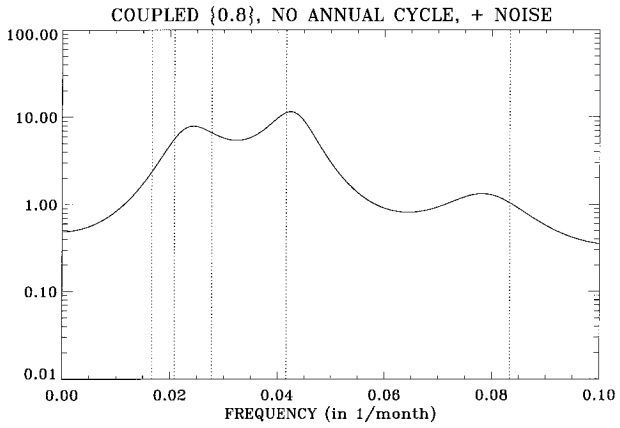

FIG. 10. Power spectrum of the Niño3 SST anomaly time series for an HCM coupled simulation with a coupling coefficient $\mu = 0.8$, with added wind stress noise and without seasonal cycle. Length for the time series is 41 yr.

the seasonal cycle is set by the deterministic frequency locking behavior, and the addition of a reasonable estimate of the noise does not mask this property.

5. Can noise sustain a decaying ENSO mode?

Within the framework of bifurcation theory, the HCM follows a Hopf bifurcation from a stable climatological state (for weak values of the coupling coefficient μ) to an ENSO-like behavior (for stronger values of μ): sustained interannual variability of realistic amplitude occurs around $\mu = 1.2$. The atmospheric noise appears essential only to give aperiodicity to the phenomenon. We discuss in this section another possible scenario for the occurrence of sustained interannual variability in the model: the coupling coefficient is now chosen below the Hopf bifurcation, so the ENSO mode decays with time in absence of noise. We test the ability of atmospheric noise to sustain interannual variability in the model in this stable case. Qualitatively, we expect from the properties of linear stable stochastic systems (e.g., Jazwinski 1970) that addition of noise will produce a peak at the frequency of the ENSO mode if it is not too strongly damped. The question is, quantitatively, are the amplitude and other properties of the variability sufficiently similar to observed that this is a viable explanation? We know in advance that this depends strongly on the coupling coefficient, since for the uncoupled case there is no model ENSO peak (Fig. 2).

Our results in Fig. 10 show that an additive stochastic component on the atmospheric forcing is able to produce sustained interannual variability of plausible amplitude when the coupling is reasonably strong ($\mu = 0.8$), even when the ENSO mode is stable. The amplitude of the resulting oscillations is, however, somewhat smaller than an equivalent standard case ($\mu = 1.2$, no seasonal cycle). The standard deviation associated with the Niño3 SST anomaly signal is here a convenient index to compare the different types of variability (see Table 2). This index deduced from the 1950–93 observed time series for the Niño3 index is 0.82°C. The value we get from our most realistic experiment (with noise and seasonal cycle included) almost matches it (0.84°C). The standard deviation in the current case ($\mu = 0.8$, with noise and no seasonal cycle) happens to be of the same magnitude (0.80°C) but must be compared with the standard case without seasonal cycle (0.98°C) and thus is noticeably smaller.

This tends to make the hypothesis of a ''noise-sustained ENSO variability'' (with an inherent behavior below the Hopf bifurcation) weaker than the one of a ''naturally oscillating mode'' (above the Hopf bifurcation). Moreover, it is worth noting that we studied here a scenario with a coupling coefficient μ chosen just below the bifurcation point, and other relevant (smaller) choices for μ would have led to even smaller and less

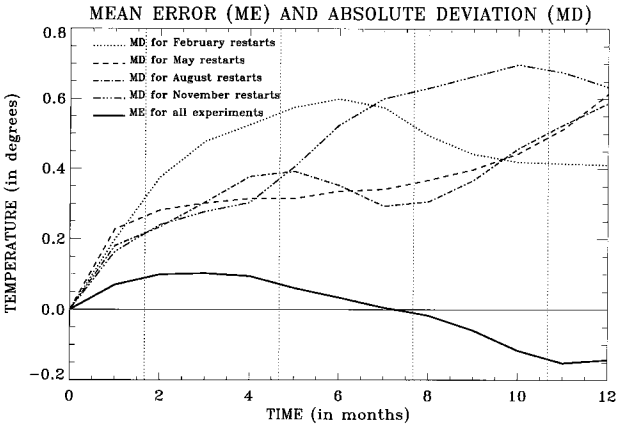

FIG. 11. Mean error (ME) and absolute deviation (MD) for the Niño3 SST anomaly index in the 132 1-year hindcast experiments. The mean error (solid line) corresponds to the whole ensemble of experiments, while the mean absolute deviation is given seasonally.

realistic amplitudes. However, we cannot rule out this hypothesis at this time.

6. Effects on predictability

a. Model–model forecasts

We use in this section an ensemble of model–model prediction experiments to test the effects of atmospheric noise on ENSO predictability. Our model forecasts consist of 132 1-yr coupled experiments with noise and seasonal cycle included. Initial conditions for the forecasts are provided by randomly selected ocean states from our 88-year coupled integration with noise and prescribed seasonal cycle. Multiple restarts are run by changing either the initial conditions or the time series used for noise: the forecasts are initialized with 16 different initial conditions (four randomly selected February, May, August, and November calendar months) and each initial condition is run with eight different noise time series.

These forecasts may be considered as other possible realizations of the coupled behavior found in the control experiment that provided their initial conditions. They ask the question, how sensitive is the evolution of the system from given ocean initial conditions to different evolutions of the atmospheric internal variability? For each model forecast, we compute departures from the control simulation, month after month. Because this procedure gives privileged status to one realization (the control run), we check that the mean of the forecast ensemble does not differ too greatly from the control. This ''mean error,'' exactly zero for a zero-month lag because of the definition for the initial conditions, does not show any particular growth with time when averaged for the whole set of noise experiments, as shown for the Niño3 SST anomaly index in Fig. 11 (solid line). Its overall small value (less than 0.15°C for up to 12-month lags) indicates that the control can indeed be considered a ''typical'' realization.

b. Loss of predictability associated with stochastic forcing

The growth with time (i.e., with the value of the forecast lead expressed in months) of the mean absolute deviation of the hindcasts from their average is a measure of the predictability of the ENSO variability simulated by the model: the faster the growth, the weaker the predictability. A fast dispersion, defined with respect to the mean of all hindcast experiments, indeed indicates a strong dependence of the hindcasts' results on the atmospheric noise. As a measure of this dispersion, we choose the following measure of mean deviation:

$$MD(m) = \frac{1}{N}\sum_{i=1}^{N}\left[\Delta T_i(m) - \frac{1}{N}\sum_{i=1}^{N}\Delta T_i(m)\right], \quad (6.1)$$

where $\Delta T_i(m)$ is the Niño3 SST anomaly (with respect to the reference experiment) for month m of hindcast i, with N being the number of hindcasts considered in the subset.

As shown in Fig. 11, for all seasonal subsets of noise experiments the mean deviation generally increases with time (almost linearly for the first months), and its upper range after 12 months roughly corresponds to the amplitude of the Niño3 SST anomalies in the control run. The worst case for rapid dispersion is obtained for restarts in February, with mean deviation of 0.6°C attained at 5 months. For May and August restarts, the mean deviation does not exceed 0.4°C until the tenth month of forecast lead. For November forecasts 0.4°C is exceeded at 5 months. These results are consistent with the results obtained by Kleeman and Power (1994) in their study of the limits of predictability by stochastic forcing in a simpler coupled model.

Other studies (Balmaseda et al. 1995) have pointed out that ENSO SST predictability appears to have a minimum in spring and a maximum in summer, at least when the degree of phase locking to the annual cycle is high. Springtime is characterized by a weak coupling between the surface and the subsurface ocean because the thermocline is quite flat along the equator (and thus deep in the eastern Pacific). Applied to the case here, we would postulate that local, short-term fluctuations induced by atmospheric noise are more effective during spring, as opposed to summertime when the coupling with the subsurface ocean favors connection to the more slowly evolving part of the system. It is worth noting that our hindcast experiments initiated in November are highly sensitive to the noise roughly six months after their start, right in springtime. The same phenomenon, though attenuated, is noticeable for hindcasts initiated in August and May too, respectively, at lags 9 and 12 months.

7. A rough test of multiplicative noise

While quantitative estimation of a suitable additive uncoupled wind stress noise is challenging, estimating the degree of multiplicative noise from observations is even more difficult (e.g., Penland and Matrosova 1994). By multiplicative noise, we mean stochastic effects of the form $\xi F(X)$ where X is the state vector of the system, ξ is a random variable, and F a vector function. In our case, only SST affects the atmosphere, and the deterministic part of the atmosphere is slaved to the ocean, so X is just the SST field and F can plausibly be taken as linear at leading order. We further know from physical considerations that the atmospheric boundary layer moist static equation, using bulk formulas for evaporation and sensible heat, has the form

$$\rho_a c_D \mathrm{V} h_a + (\text{large scale dynamics}) = \rho_a c_D \mathrm{V} h_{sat}(T_s),$$

where V is the wind speed, h the atmospheric boundary layer moist static energy, and h_{sat} the saturation value of moist static energy evaluated at the sea surface temperature T_s. The effective coupling of ocean to atmosphere thus depends on wind speed, which has substantial stochastic fluctuations about its mean value, and these multiply SST perturbations. While we have estimated the part of atmospheric variability that does not depend on SST, it is desirable to have some feel for whether such multiplicative effects are important. Ignoring the spatial variations of these effects, the simplest form of a multiplicative noise is to replace the deterministic coupling coefficient μ, by a coupling that contains a noise component: $\mu(1 + m\xi)$ where ξ is a scalar random variable. In the atmospheric model, winds thus depend on SST by a factor that fluctuates about the deterministic value. We choose ξ from a uniform distribution on the interval $(-1, 1)$, and apply it monthly, that is, we assume correlation on timescales up to a month, white on longer timescales. We show the case with scaling factor m = 0.3, that is, very substantial fluctuations of up to 30% about the mean value. If the deterministic coupling coefficient were varied over such a range, the ENSO behavior would move from heavily damped to unrealistically large oscillations. Given this, we were surprised at the weakness of the model sensitivity to this noise. For a run with this multiplicative noise, in a case with no seasonal cycle, the spectra in Fig. 12 shows little peak broadening or shifting compared to the control run of Fig. 6a. This is encouraging since it suggests that accurate depiction of the multiplicative noise is a less burning issue than we had initially feared.

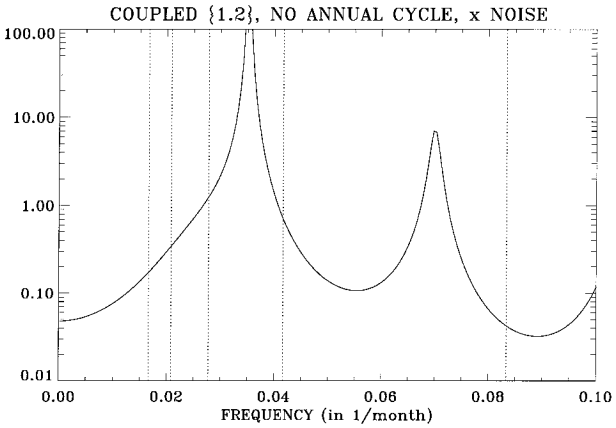

FIG. 12. As in Fig. 6a except for the simulation with a multiplicative noise component (modified coupling coefficient). Length of the time series is 42 yr.

8. Summary and conclusions

We have attempted to quantify the hypothesis that ''weather noise''—atmospheric internal variability with short decorrelation times—contributes to the irregularity and loss of predictability in ENSO. A hybrid coupled model of ENSO was used, with an estimate of the atmospheric additive stochastic forcing by wind stress. The crucial feature is that the noise spatial correlations and magnitude are obtained empirically from the FSU wind stress dataset, in a manner constructed to be consistent with the empirical feedback used for the wind stress in the deterministic part of the atmospheric model. The atmospheric model is used to remove the part of the FSU wind stress that can be attributed deterministically to SST (by linear methods). The remainder of the atmospheric variability is then attributed to stochastic forcing by internal atmospheric variability and other effects not included in the deterministic part of the coupled system. These residual fields (after removal of SST-related signal) are reasonably well decorrelated on timescales longer than a month, consistent with the physical hypothesis. To create the stochastic forcing, we simply make random picks among the maps of residual fields, in a manner that is white in time on scales longer than a month. This preserves the variance of the observed fields, as well as the spatial correlations, which is important since the ocean is sensitive to the spatial structure of forcing fields. We ignore the detailed decorrelation structure of weather noise in timescales shorter than a month, on the assumption that this will not matter to the interannual behavior.

The main caveat on this estimate of the weather noise is that we cannot distinguish genuine uncoupled atmospheric variability from observational errors. We cannot tell whether the variance is over- or underestimated, since observational errors can both omit some of the true atmospheric variability or introduce erroneous variance. All conclusions are thus contingent on the quality of the FSU dataset. Zebiak (1990) has pointed out that the FSU analysis can be problematic in those regions of the Pacific nearly devoid of observations. Concerns with representing the atmospheric internal variability as a purely additive stochastic forcing were allayed by a sensitivity test in which a rough represen-

tation of multiplicative noise was shown to have relatively small effects in the coupled model.

When the wind stress noise product is added to the uncoupled ocean model, it produces a spectrum of eastern equatorial SST that is roughly white on timescales longer than a year. The coupled model has a sharp interannual spectral peak in absence of stochastic forcing due to the sustained ENSO cycle produced by coupling. The sensitivity of this cycle to addition of the wind stress noise was investigated in cases with annual average conditions and cases with the seasonal cycle included. The simulated interannual variability for experiments with wind stress noise is much more irregular and is associated with a much broader ENSO-related spectral peak than in no-noise cases. Although our model ENSO period is shorter than observed, the qualitative features of peak broadening should be robust to this. Noise also was found to shift the peak toward lower frequencies in the case with seasonal cycle. The way individual ENSO events develop, when they do not abort before complete maturity, is generally consistent with the pattern obtained in absence of noise: there is some added variety in the spatial pattern in presence of noise, but the phenomenon is basically the same. Preferential seasonal phase locking comparable to that found in observations, still occurs in presence of noise.

The stochastic forcing was used to investigate the limits of ENSO predictability associated with atmospheric weather noise. The noise-related error growth in model–model forecast comparisons is found to be substantial. Loss of skill occurs within about half an ENSO cycle. Although the caveats on the model ENSO frequency imply caution in interpreting the timescale of loss of predictability, we can state with some confidence that the weather noise limit to predictability will be a significant factor to contend with in pushing ENSO predictions to longer lead times. We note also that the limitation imposed by weather noise differs from many other sources of error in that it cannot be improved by better model initialization.

Additional noise experiments were also performed with subcritical values of the coupling coefficient, that is, values slightly smaller than is required for the ENSO cycle to arise by instability of the basic state. The addition of noise can sustain variability associated with the model ENSO mode with a broad spectral peak. The variance is slightly too small compared with observations, but this is parameter dependent. From the present results, we must admit the possibility that ENSO is a stable oscillation maintained by noise. However, the coupling must be strong enough that the oscillation is only slowly decaying. Jin et al. (1996) postulate that more detailed spectral signatures associated with secondary peaks favor the hypothesis of an unstable ENSO mode, but we cannot apply this to current results. Our model results do differ from the Penland and Sardeshmukh (1995) hypothesis of noise-forced modes estimated from SST data in that the spectral peak is clearly associated with the single ENSO mode that goes unstable at higher coupling.

Because the question of the effects of weather noise in ENSO must be settled quantitatively, we expect much future work will be required to refine these estimates. We have noted a number of caveats in the present results, despite careful attention to separating noise from coupled signal in our data analysis. Questions of model dependence are aided by the similarity of the conclusions presented here and companion results by Eckert and Latif (1997) using a different model and different approach to the stochastic forcing.

Our results emphasize the importance of atmospheric random variability in understanding ENSO irregularity and limits to ENSO predictability. This does not dismantle other explanations based on chaos within the slow component of the coupled system. In fact, the richer variability (a larger spectral peak) obtained with noise in cases including the earth's seasonal cycle is likely connected with such nonlinear subharmonic resonance phenomena. In the real coupled system, both effects—atmospheric noise and transition to chaos—may contribute to ENSO irregularity. It is difficult to distinguish between these mechanisms with available time series. If forced to choose, based on our present results, we would opt for the noise.

Acknowledgments. This study was supported in part by grants from the National Oceanographic and Atmospheric Administration NA46GP0244 and NA56GP0451 (BB and JDN) and NA66GP0195 (DG). During this study BB also received support from the Centre National de la Recherche Scientifique. Earlier versions of this work were presented at the American Geophysical Union conference in December 1993 and at the International TOGA Scientific Conference in April 1995.

REFERENCES

Balmaseda, M. A., M. K. Davey, and D. L. T. Anderson, 1995: Decadal and seasonal dependence of ENSO prediction skill. *J. Climate,* **8,** 2705–2715.

Barnett, T. P., 1985: Variations in near-global sea level pressure. *J. Atmos. Sci.,* **42,** 478–501.

——, 1991: The interaction of multiple time scales in the tropical climate system. *J. Climate,* **4,** 269–285.

——, M. Latif, N. Graham, M. Flügel, S. Pazan, and W. White, 1993: ENSO and ENSO-related predictability. Part I: Prediction of equatorial Pacific sea surface temperature with a hybrid coupled ocean–atmosphere model. *J. Climate,* **6,** 1545–1566.

——, and Coauthors, 1994: Forecasting global ENSO-related climate anomalies. *Tellus,* **46A,** 381–397.

Battisti, D. S., 1988: Dynamics and thermodynamics of a warming event in a coupled tropical atmosphere–ocean model. *J. Atmos. Sci.,* **45,** 2889–2919.

——, and A. C. Hirst, 1989: Interannual variability in the tropical atmosphere/ocean system: Influence of the basic state, ocean geometry, and nonlinearity. *J. Atmos. Sci.,* **46,** 1687–1712.

Bretherton, C. S., C. Smith, and J. M. Wallace, 1992: An intercomparison of methods for finding coupled patterns in climate data. *J. Climate,* **5,** 541–560.

Chang, P., B. Wang, T. Li, and L. Ji, 1994: Interactions between the

seasonal cycle and the Southern Oscillation—Frequency entrainment and chaos in a coupled ocean–atmosphere model. *Geophys. Res. Lett.,* **21,** 2817–2820.

——, L. Ji, B. Wang, and T. Li, 1995: Interactions between the seasonal cycle and El Niño–Southern Oscillation in an intermediate coupled ocean–atmosphere model. *J. Atmos. Sci.,* **52,** 2353–2372.

Deser, C., and J. M. Wallace, 1990: Large-scale atmospheric circulation features of warm and cold episodes in the tropical Pacific. *J. Climate,* **3,** 1254–1281.

Dettinger, M. D., M. Ghil, C. M. Strong, W. Weibel, and P. Yiou, 1995: Software expedites singular-spectrum analysis of noisy time series. *Eos, Trans. Amer. Geophys. Union,* **76,** 12, 14, 21.

Eckert, C., and M. Latif, 1997: Predictability of a stochastically forced hybrid coupled model of the tropical Pacific ocean–atmosphere system. *J. Climate,* **10,** 1488–1504.

Gill, A. E., 1980: Some simple solutions for heat-induced tropical circulation. *Quart. J. Roy. Meteor. Soc.,* **106,** 447–462.

Goswami, B. N., and J. Shukla, 1991: Predictability of a coupled ocean–atmosphere model. *J. Climate,* **4,** 3–22.

Hirst, A. C., 1986: Unstable and damped equatorial modes in simple coupled ocean–atmosphere models. *J. Atmos. Sci.,* **43,** 606–630.

——, 1988: Slow instabilities in tropical ocean basin-global atmosphere models. *J. Atmos. Sci.,* **45,** 830–852.

Iooss, G., and D. D. Joseph, 1990: *Elementary Stability and Bifurcation Theory.* Springer-Verlag, 324 pp.

Jazwinski, A. H., 1970: *Stochastic Processes and Filtering Theory.* Academic Press, 376 pp.

Jiang, N., J. D. Neelin, and M. Ghil, 1995: Quasi-quadrennial and quasi-biennial variability in COADS equatorial Pacific sea surface temperature and winds. *Climate Dyn.,* **12,** 101–112.

Jin, F.-F., and J. D. Neelin, 1993a: Modes of interannual tropical ocean–atmosphere interaction—A unified view. Part I: Numerical results. *J. Atmos. Sci.,* **50,** 3477–3503.

——, and ——, 1993b: Modes of interannual tropical ocean–atmosphere interaction—A unified view. Part III: Analytical results in fully coupled cases. *J. Atmos. Sci.,* **50,** 3523–3540.

——, ——, and M. Ghil, 1994: El Niño on the Devil's staircase: Annual subharmonic steps to chaos. *Science,* **264,** 70–72.

——, ——, and ——, 1996: El Niño/Southern Oscillation and the annual cycle: Subharmonic frequency locking and aperiodicity. *Physica D,* **9,** 442–465.

Kleeman, R., and S. B. Power, 1994: Limits to predictability in a coupled ocean–atmosphere model due to atmospheric noise. *Tellus,* **46A,** 529–540.

Latif, M., and M. Flügel, 1991: An investigation of short-range climate predictability in the tropical Pacific. *J. Geophys. Res.,* **96,** 2661–2673.

——, A. Sterl, E. Maier-Reimer, and M. M. Junge, 1993: Climate variability in a coupled GCM. Part I: The tropical Pacific. *J. Climate,* **6,** 5–21.

Legler, D. M., and J. J. O'Brien, 1984: *Atlas of Tropical Pacific Wind-Stress Climatology 1971–1980.* The Florida State University, 182 pp.

Mantua, N. J., and D. S. Battisti, 1995: Aperiodic variability in the Zebiak–Cane coupled ocean–atmosphere model: Air–sea interactions in the western equatorial Pacific. *J. Climate,* **8,** 2897–2927.

Münnich, M., M. A. Cane, and S. E. Zebiak, 1991: A study of self-excited oscillations of the tropical ocean–atmosphere system. Part II: Nonlinear cases. *J. Atmos. Sci.,* **48,** 1238–1248.

Neelin, J. D., 1990: A hybrid coupled general circulation model for El Niño studies. *J. Atmos. Sci.,* **47,** 674–693.

——, 1991: The slow sea surface temperature mode and the fast-wave limit: Analytic theory for tropical interannual oscillations and experiments in a hybrid coupled model. *J. Atmos. Sci.,* **48,** 584–606.

——, and F.-F. Jin, 1993: Modes of interannual tropical ocean–atmosphere interaction—A unified view. Part II: Analytical results in the weak coupling limit. *J. Atmos. Sci.,* **50,** 3504–3522.

——, and Coauthors, 1992: Tropical air–sea interaction in general circulation models. *Climate Dyn.,* **7,** 73–104.

Oberhuber, J. M., 1988: An atlas based on the COADS data set: The budget of heat, buoyancy, and turbulent kinetic energy at the surface of the global ocean. MPI Rep. 15, 13 pp. [Available from Max-Planck-Institut für Meteorologie, Hamburg, Bundestrasse 55, D-2000, Germany.]

Paulson, C. A., and J. J. Simpson, 1977: Irradiance measurements in the upper ocean. *J. Phys. Oceanogr.,* **7,** 952–956.

Penland, C., and L. Matrosova, 1994: A balance condition for stochastic numerical models with application to the El Niño–Southern Oscillation. *J. Climate,* **7,** 1352–1372.

——, and P. D. Sardeshmukh, 1995: The optimal growth of tropical sea surface temperature anomalies. *J. Climate,* **8,** 1999–2024.

Peters, H., M. C. Gregg, and J. M. Toole, 1988: On the parameterization of the equatorial turbulence. *J. Geophys. Res.,* **93,** 1199–1218.

Philander, S. G. H., T. Yamagata, and R. C. Pacanowski, 1984: Unstable air–sea interactions in the tropics. *J. Atmos. Sci.,* **41,** 604–613.

——, R. C. Pacanowski, N. C. Lau, and M. J. Nath, 1992: Simulation of ENSO with a global atmospheric GCM coupled to a high resolution, tropical Pacific Ocean GCM. *J. Climate,* **5,** 308–329.

Rasmusson, E. M., and T. H. Carpenter, 1982: Variations in tropical sea surface temperature and surface wind fields associated with the Southern Oscillation / El Niño. *Mon. Wea. Rev.,* **110,** 354–384.

——, X. Wang, and C. F. Ropelewski, 1990: The biennial component of ENSO variability. *J. Mar. Syst.,* **1,** 71–96.

Reynolds, R. W., 1988: A real-time global sea surface temperature analysis. *J. Climate,* **1,** 75–86.

Ropelewski, C. F., and M. S. Halpert, 1989: Precipitation patterns associated with the high index phase of the Southern Oscillation. *J. Climate,* **2,** 594–614.

Schopf, P. S., and M. J. Suarez, 1988: Vacillations in a coupled ocean–atmosphere model. *J. Atmos. Sci.,* **45,** 549–566.

——, and ——, 1990: Ocean wave dynamics and the time scale of ENSO. *J. Phys. Oceanogr.,* **20,** 629–645.

Seager, R., S. E. Zebiak, and M. A. Cane, 1988: A model of the tropical Pacific sea surface temperature climatology. *J. Geophys. Res.,* **93,** 1265–1280.

Syu, H.-H., J. D. Neelin, and D. S. Gutzler, 1995: Seasonal and interannual variability in a hybrid coupled GCM. *J. Climate,* **8,** 2121–2143.

Tziperman, E., L. Stone, M. A. Cane, and H. Jarosh, 1994: El Niño chaos: Overlapping of resonances between the seasonal cycle and the Pacific ocean–atmosphere oscillator. *Science,* **264,** 72–74.

——, M. A. Cane, and S. Zebiak, 1995: Irregularity and locking to the seasonal cycle in an ENSO prediction model as explained by the quasi-periodicity route to chaos. *J. Atmos. Sci.,* **52,** 293–306.

Wakata, Y., and E. S. Sarachik, 1991a: On the role of equatorial ocean modes in the ENSO cycle. *J. Phys. Oceanogr.,* **21,** 434–443.

——, and ——, 1991b: Unstable coupled atmosphere–ocean basin modes in the presence of a spatially varying basic state. *J. Atmos. Sci.,* **48,** 2060–2077.

Waliser, D. E., B. Blanke, J. D. Neelin, and C. Gautier, 1994: Shortwave feedbacks and ENSO: Forced ocean and coupled ocean–atmosphere experiments. *J. Geophys. Res.,* **99,** 25 109–25 125.

Wyrtki, K., 1985: Water displacements in the Pacific and the genesis of El Niño cycles. *J. Geophys. Res.,* **90,** 7129–7132.

Zebiak, S. E., 1989: On the 30–60 day oscillation and the prediction of El Niño. *J. Climate,* **2,** 1381–1387.

——, 1990: Diagnostic studies of Pacific surface winds. *J. Climate,* **3,** 1016–1031.

——, and M. A. Cane, 1987: A model El Niño–Southern Oscillation. *Mon. Wea. Rev.,* **115,** 2262–2278.